

## INORGANIC CHEMISTRY

An all-metal fullerene:  $[K@Au_{12}Sb_{20}]^{5-}$ Yu-He Xu<sup>1</sup>, Wen-Juan Tian<sup>2</sup>, Alvaro Muñoz-Castro<sup>3</sup>, Gernot Frenking<sup>4,5</sup>, Zhong-Ming Sun<sup>1\*</sup>

The  $C_{60}$  fullerene molecule has attracted tremendous interest for its distinctive nearly spherical structure. By contrast, all-metal counterparts have been elusive: Fullerene-like clusters composed of noncarbon elements typically suffer from instability, resulting in more compact geometries that require multiple embedded atoms or external ligands for stabilization. In this work, we present the synthesis of an all-metal fullerene cluster,  $[K@Au_{12}Sb_{20}]^{5-}$ , using a wet-chemistry method. The cluster's structure was determined by single crystal x-ray diffraction, which revealed a fullerene framework consisting of 20 antimony atoms. Theoretical calculations further indicate that this distinct cluster exhibits aromatic behavior.

The study of all-metal clusters reveals the delicate balance between electronic shells and structural geometry: The quantum confinement of electrons (1, 2) gives rise to a rich diversity of atomic arrangements with intriguing bonding characteristics (3–5). The discovery of buckminsterfullerene ( $C_{60}$ ), which marked a major milestone in the exploration and application of stable three-dimensional cages, has sprouted new research disciplines in chemical, physical, and material science (6, 7). The distinct near-spherical structure of fullerenes along with the surface of delocalized  $\pi$  electrons produces many notable properties and enables a wide range of applications in biology, medicine, electronics, and photovoltaics (8, 9). What's more, the internal cavity of fullerenes provides a space for hosting a variety of atoms and molecules, giving rise to a class of endohedral clusters termed endofullerenes (10–13). The rapid progress in fullerene-related clusters and extensive applications of fullerene-based materials have

prompted the exploration of analogous hollow sphere molecules composed of other main-group or transition metal elements known as inorganic fullerenes (14).  $In_{74}$  with  $D_{3h}$  symmetry and  $In_{48}Na_{12}$  with  $D_{3d}$  symmetry are fullerene-like constructs found in the solid-state Zintl phase  $Na_{96}In_{97}Z_2$  ( $Z = Ni, Pd, Pt$ ); both constitute the outermost shell of a four-layer onion-like structure rather than existing as hollow cages (15). Additionally, theoretical calculations have predicted the stability of an all-gold fullerene  $Au_{32}$ , structurally very similar to  $C_{60}$  (16). However, experiments produced an  $Au_{32}^{8+}$  cluster featuring a compact configuration of  $Au_{12}@Au_{20}$ , which was different from the previously anticipated fullerene, and the cationic cluster was protected by organic ligand (17, 18). Another ligand-protected dodecahedral silafulfullerane was also reported, which encapsulated one chloride ion (19). Obtaining ligand-free  $C_{60}$  analogs with heavier atoms may be constrained by their susceptibility to rearrangement into alternative, more stable

structures, as evidenced by previous theoretical studies. In this work, we report the isolation and characterization of an all-metal endohedral fullerene,  $[K@Au_{12}Sb_{20}]^{5-}$  through a solution-based method in which only one  $K^+$  ion resides in a bare dodecahedral cage comprising 12 Au and 20 Sb atoms with distinct structural features. Each Au atom sits in the center of an Sb pentagonal plane without breaking the structure of  $Sb_{20}$  cage, but rather stretching the cage size. The  $[K@Au_{12}Sb_{20}]^{5-}$  cluster is held together exclusively by Au–Sb bonds exploiting the icosahedron-dodecahedron duality, thereby retaining an icosahedral, near-spherical geometry with similar size to  $C_{60}$ , but composed of 32 atoms.

## Synthesis and characterization

Compound  $[K(2,2,2\text{-crypt})]_5[K@Au_{12}Sb_{20}]$  was synthesized by reacting the Zintl phase  $K_8SnSb_4$  with precursor  $Au(PPh_3)Me$  in an ethylenediamine solution, which was facilitated by the presence of  $[2.2.2]crypt$  (see the supplementary materials). After stirring at room temperature for 7 hours, the color of the reaction

<sup>1</sup>State Key Laboratory of Elemento-Organic Chemistry, Tianjin Key Lab of Rare Earth Materials and Applications, School of Materials Science and Engineering, Nankai University, Tianjin 300350, China. <sup>2</sup>Institute of Molecular Science, Shanxi University, Taiyuan 030006, China. <sup>3</sup>Facultad de Ingeniería, Arquitectura y Diseño, Universidad San Sebastián, Bellavista 7, Santiago 8420524, Chile. <sup>4</sup>Institute of Advanced Synthesis, School of Chemistry and Molecular Engineering, State Key Laboratory of Materials-Oriented Chemical Engineering, Nanjing Tech University, Nanjing 211816, China. <sup>5</sup>Fachbereich Chemie, Philipps-Universität Marburg, Hans-Meerwein-Strasse 4, 35043 Marburg, Germany.

\*Corresponding author. Email: sunlab@nankai.edu.cn

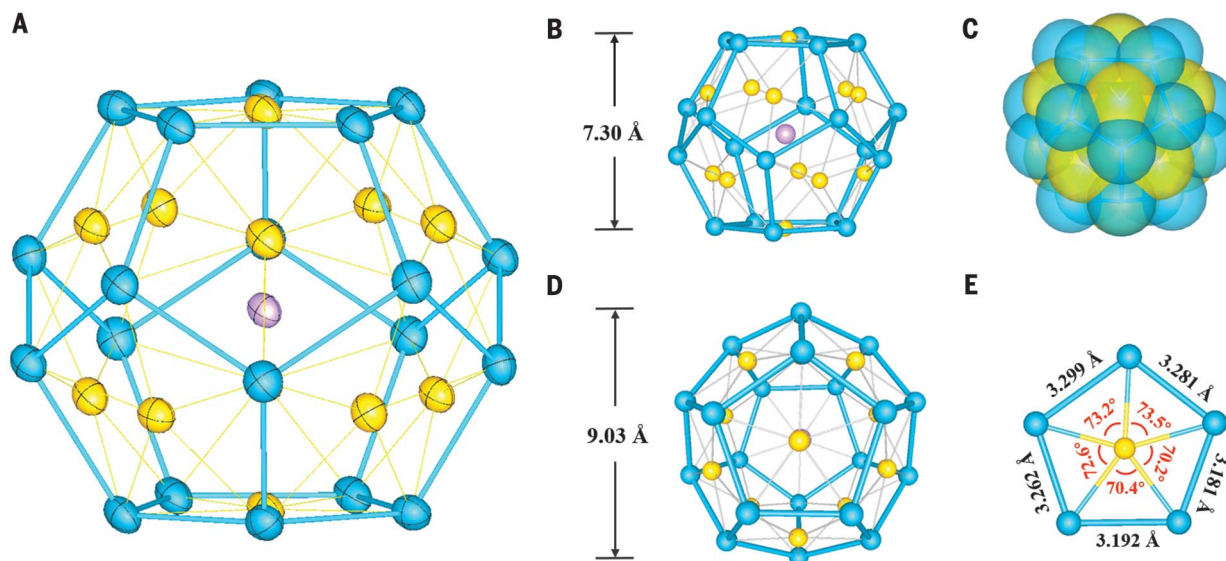


**Fig. 1. Molecular structure of the  $[K@Au_{12}Sb_{20}]^{5-}$  cluster.** (A) Thermal ellipsoid plot (50% probability) of the cluster. (B) Front side view of (A). (C) Space-filling representation of the crystal structure. (D) Top view of (A). (E) A typical  $Sb_5$  pentagon face centered by a gold atom in the cluster (with Sb–Sb bond lengths marked). K is represented by cyan, Au by gold, and Sb by blue.

mixture was observed to change from brown-red to brown-gold, and the stirring was stopped. The reaction vial was stored in a refrigerator at 10°C for about 5 days, and black block-shaped crystals were isolated from the bottom of the vial in a yield of 25% based on Au(PPh<sub>3</sub>)Me. The resulting complex was characterized by single-crystal x-ray diffraction, which revealed its crystallization in the triclinic space group *P*-1. The asymmetric unit contained five [K(2,2,2-crypt)]<sup>+</sup> charge-balancing cations. Additionally, energy-dispersive x-ray spectroscopy (EDS) was used to determine the elemental composition of the compound. The obtained atom values for Au and Sb were in good agreement with the theoretical values calculated for Au<sub>12</sub>Sb<sub>20</sub>. Many attempts were made to obtain mass spectral information, but to no avail. Because of the high negative charge of the cluster, it is extremely unstable in the air, and a distinct gray precipitate was observed in the crystal solution once exposed to air, which generated great difficulties in mass spectral detection.

As shown in Fig. 1, the anion [K@Au<sub>12</sub>Sb<sub>20</sub>]<sup>5-</sup> exhibits the overall structure of a slightly flattened dodecahedron with each Sb<sub>5</sub> pentagonal face centered by one Au atom. The average

short axis of the cage measures 7.30 Å (the distance between two opposing Au@Sb<sub>5</sub> pentagonal faces) (Fig. 1, A to C), slightly exceeding the diameter of C<sub>60</sub> (7.1 Å) (20), whereas the longest axis measures 9.03 Å (the distance between the two farthest Sb atoms on the cage) (Fig. 1D), which is comparable to the calculated diameter of the theoretically predicted Au<sub>32</sub> (9.0 Å) (16). In all twelve planes, the sum of the angles between the central Au atom and the five vertices of the Sb<sub>5</sub> ring is close to 360°, indicating that the gold atom lies on the surface of *cyclo*-Sb<sub>5</sub> (in the Sb<sub>5</sub> plane in Fig. 1E, for example, the sum of the angles is 359.9°). Such a planar pentacoordinate motif is unusual. Theoretical studies predicted a planar hexacoordinate carbon atom in the anion CB<sub>6</sub><sup>2-</sup>, which has not yet been synthesized (21). Similarly, an iron-centered planar cation [FeSb<sub>5</sub>]<sup>+</sup> was predicted, in which the Sb<sub>5</sub> ring is aromatic with equal-length Sb-Sb bonds of 2.973 Å (22). However, the Sb-Sb bond distances in [K@Au<sub>12</sub>Sb<sub>20</sub>]<sup>5-</sup> span a wide range from 3.114 to 3.436 Å (average of 3.227 Å), which are significantly longer than that of [FeSb<sub>5</sub>]<sup>+</sup> as well as typical Sb-Sb single bonds (2.81 to 2.98 Å) (23–25), denoting distinct structural features.

Additionally, the Sb<sub>20</sub> dodecahedral shell is expanded compared with that of the reported [Sb@Ni<sub>12</sub>@Sb<sub>20</sub>]<sup>−</sup> compounds (where the average Sb-Sb distance is 3.11 Å), potentially owing to the influence of the Au atom in the plane enlarging the Sb<sub>5</sub> pentagon (26). All Au-Sb bonds are located on the faces of the dodecahedron, with a relatively narrow range of 2.698 to 2.798 Å, which is considerably longer than the bonds observed in [Au<sub>2</sub>Sb<sub>16</sub>]<sup>4+</sup> (2.67 to 2.71 Å) and [Sb<sub>3</sub>Au<sub>3</sub>Sb<sub>3</sub>]<sup>3−</sup> (2.59 to 2.61 Å) (27, 28). The central K<sup>+</sup> ion is coordinated by twelve Au atoms, supporting their positioning on the Sb<sub>5</sub> faces. The K-Au contacts range between 3.493 and 3.756 Å, indicating predominantly electrostatic interactions. Nevertheless, the presence of K<sup>+</sup> as template cations remains crucial for the overall cluster stability.

### Theoretical analysis

To gain insights into the chemical bonding in the [K@Au<sub>12</sub>Sb<sub>20</sub>]<sup>5−</sup> cluster, theoretical analysis was conducted. The optimized structure for [K@Au<sub>12</sub>Sb<sub>20</sub>]<sup>5−</sup> revealed Au-Au distances of 4.002 Å, mediated by Au-Sb bonds of 2.773 Å, which compared well to the x-ray structure (Au-Au, 3.914 Å; Au-Sb, 2.747 Å). Comparison

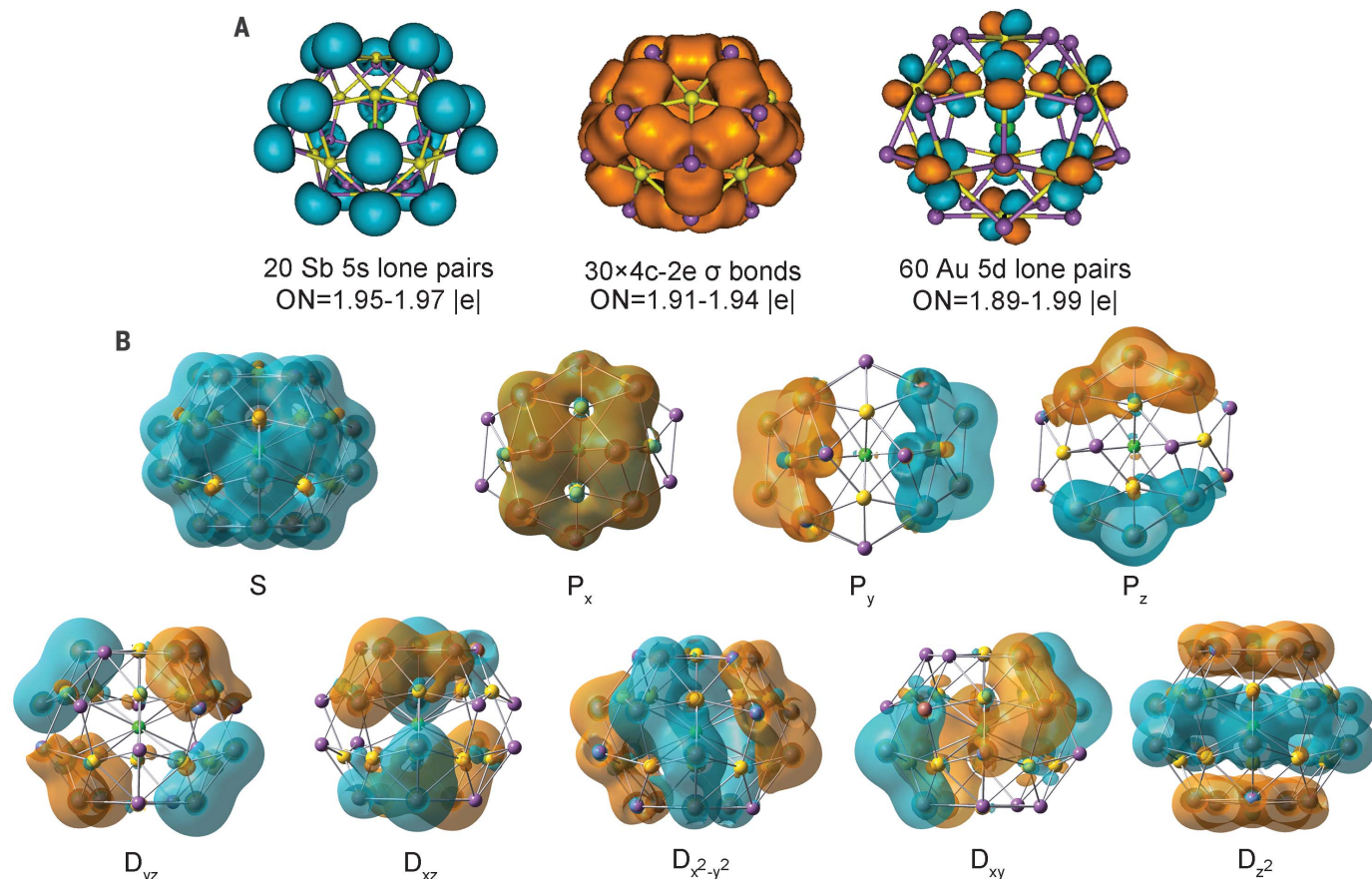


**Fig. 2.** AdNDP bonding patterns and canonical molecular orbitals for [K@Au<sub>12</sub>Sb<sub>20</sub>]<sup>5-</sup>. (A) Sb 5s, Au 5d lone pairs, and the four-center two-electron (4c-2e) σ bonds over each Sb<sub>2</sub>Au<sub>2</sub> quadrilateral. ON, occupation number. (B) Selected canonical molecular orbitals with their superatomic features (S, P, and D) indicated.



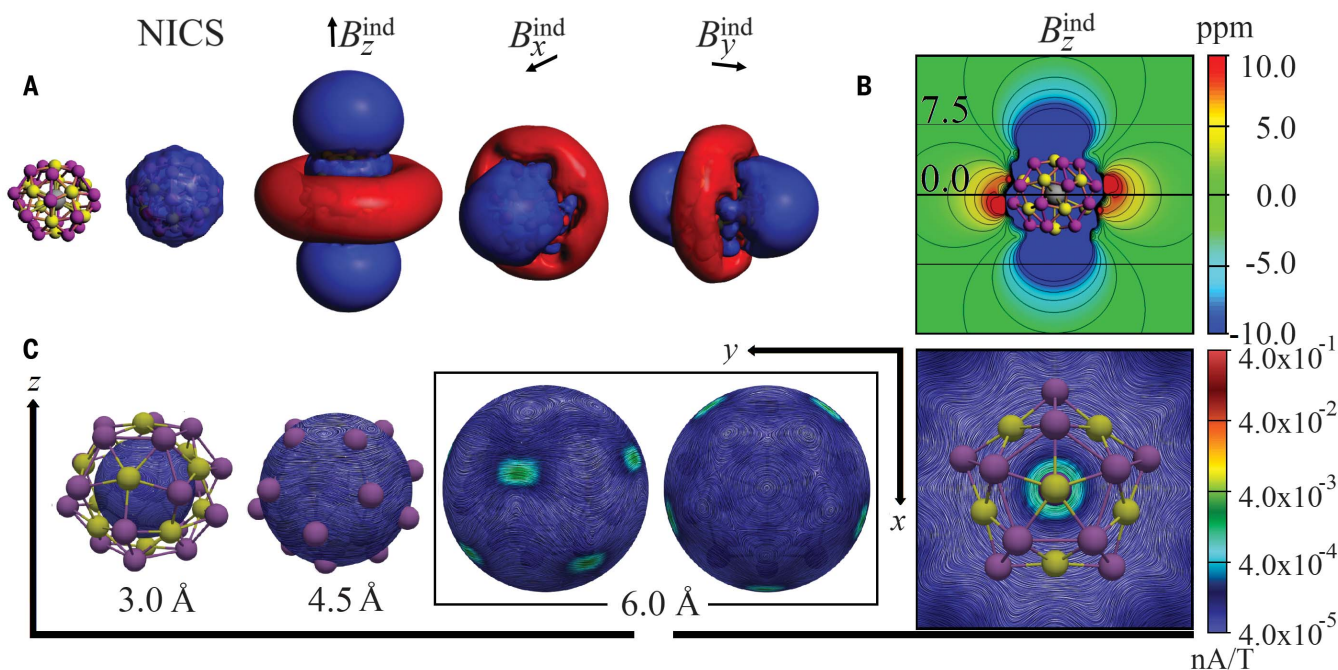


**Fig. 3. Magnetic behavior for [K@Au<sub>12</sub>Sb<sub>20</sub>]<sup>5-</sup>.** (A) Three-dimensional and (B) contour-plot representation of NICS and the induced magnetic field under certain orientations of the external field. (C) Streamline representation from GIMIC calculations of the current density over spheres with radii of 3.0, 4.5, and

6.0 Å, with the 6.0-Å sphere given in side and top views, and a cut plane at the center of the spherical cluster that denotes the magnitude of current density vector field in nA/T. Isosurface values set at  $\pm 3$  ppm. Blue represents shielding and red represents deshielding.

between the calculated energies of a  $D_{5d}$ -symmetry and  $I_h$ -symmetry structure indicated that the latter is favored by 5.4 kcal mol<sup>-1</sup>, suggesting that the experimentally characterized  $D_{5d}$ -structure may be influenced by counterions and crystal packing effects. The resulting Au<sub>12</sub> icosahedron enclosed an inner spherical cavity of diameter 7.491 Å, which is significantly larger than the Au<sub>12</sub> cage found in ligand-protected gold clusters of about 5.4 Å (29, 30). This suggests that the cage structure is supported by Au-Sb bonds, providing a larger interior volume, which thus presents a promising strategy for designing larger hollow clusters. The endohedral K<sup>+</sup> atom was stabilized by a calculated encapsulation energy of -375.8 kcal mol<sup>-1</sup>, which was primarily driven by electrostatic interactions that accounted for 90% of the stabilizing forces (table S6). The calculated highest occupied molecular orbital-lowest occupied molecular orbital (HOMO-LUMO) gap amounted to 2.57 eV at the hybrid PBE0 level. Vibrational analysis denoted a bouncing motion for the endohedral K<sup>+</sup> atom between 70 and 30 cm<sup>-1</sup>. A theoretical comparison between [K@Au<sub>12</sub>Sb<sub>20</sub>]<sup>5-</sup> and its hypothetical compact counterpart with Au-Au distances of 3.045 Å (fig. S7b) reveals an energetic preference for the characterized structure of 55.9 kcal mol<sup>-1</sup>.

To effectively allocate the 238 valence electrons, we used the adaptive natural partitioning (AdNDP) analysis with the AdNDP 2.0 code (31). The advantage of using the AdNDP method is its capacity to elucidate the chem-

ical bonding arrangement, encompassing both Lewis bonding constituents [including lone pairs (1c2e) and two-center two-electron (2c2e) bonds] and delocalized bonding constituents. In addition to the 20 Sb 5s lone pairs and 60 Au 5d lone pairs, there are 30 pairs of 4c-2e  $\sigma$  bonds distributed evenly over each butterfly-shaped Au<sub>2</sub>Sb<sub>2</sub> quadrilateral, covering the surface of the [K@Au<sub>12</sub>Sb<sub>20</sub>]<sup>5-</sup> cluster (Fig. 2A). The occupation numbers of these bonds range from 1.91 to 1.94 |e|. The remaining 18 electrons are allocated to nine orbitals with superatomic features (S, P, and D), satisfying the 3D aromatic requirement of  $2(n+1)^2$  ( $n=2$ ) (Fig. 2B). These electron distributions contribute to the overall stability and distinct properties of the cluster. The natural atomic orbitals analysis provided valuable insights into the contribution of each atom to the orbitals (32). Table S4 presents the total contribution of each atom to these orbitals, revealing that nearly all atoms make substantial contributions.

The natural population analysis conducted on the optimized structure of [K@Au<sub>12</sub>Sb<sub>20</sub>]<sup>5-</sup> revealed that the central K atom carries a charge of +0.85 |e|, indicating the presence of electrostatic interactions between the inner K atom and the outer Au<sub>12</sub>Sb<sub>20</sub> shell. Moreover, the detailed energy decomposition analysis results at the PBE0/STO-TZ2P-ZORA level, as shown in table S6, further support the ionic nature of the system. The analysis revealed that electrostatic interactions dominate the K<sup>+</sup>-cage bonding, contributing more significantly ( $\Delta E_{elstat}$

89.6%) compared with orbital interactions ( $\Delta E_{orb}$ , 7.4%) in attracting local charges and stabilizing the system.

To evaluate the aromatic properties of [K@Au<sub>12</sub>Sb<sub>20</sub>]<sup>5-</sup>, the overall magnetic behavior was given by the three-dimensional representation of nucleus-independent chemical shift (NICS) which accounted for the orientationally averaged behavior resulting from the experimental molecular tumbling in solution (Fig. 3). The NICS isosurface exhibits a shielding contour at the spherical cage, which suggests a spherical aromatic behavior (33, 34). To overcome the NICS exaltation near to heavy nuclei, we focused our analysis on the long-range characteristics of the induced magnetic field at the low-electron density limit. (35) Moreover, the representation of the magnetic response under specific orientation of the external field ( $B_i^{ind}$ ;  $i = x, y, z$ ) provides a picture of the shielding and deshielding regions that account for the possible global aromatic characteristics in [K@Au<sub>12</sub>Sb<sub>20</sub>]<sup>5-</sup>. As a result, from  $B_z^{ind}$ , an enhanced long-range shielding region aligned to the applied field for different orientations was obtained, complemented with a deshielding region in a perpendicular plane, which accounts for the shielding cone property inherent to aromatic species (29, 36). The long-range shielding region exhibited calculated values of -20.0 ppm at 7.5 Å from the center of the structure, and of -2.6 ppm at 15.0 Å (Fig. 3b), thus supporting the spherical aromatic behavior of [K@Au<sub>12</sub>Sb<sub>20</sub>]<sup>5-</sup> and leading to an enhanced

shielding region. In addition, the current density upon a *z*-aligned external field was given from gauge-including magnetically induced currents (GIMIC) calculations, denoting a collective of parallel currents around the cluster that were observed at inner regions (3.0 Å of radius), at the structure contour (4.5 Å), and outside of the spherical shell. This analysis supports the formation of a long-range shielding region owing to the presence of aromatic currents upon an external field. Integration of the induced current strength denoted values of 9.8 nanoamperes per tesla (nA/T), contributed by +158.4 nA/T from diatropic and −148.6 nA/T from paratropic currents, which is sizable in comparison to the prototypical planar aromatic species given by benzene, with a value of 12.1 nA/T at the PBE0/def2-tpvz level. At the PBE0/LanL2DZ level, a value of 21.2 nA/T was obtained, denoting dependence of the level of theory.

The Au–Sb heterobonds play a crucial role in maintaining the structural integrity of the cage, whereas the endohedral cation acts as a template for structure formation. Future investigations will focus on exploring alternative synthetic strategies that leverage the interplay between cage composition and endohedral templates, thereby enabling the rational and controlled synthesis of larger all-metal fullerenes. These superatoms hold great potential for the design and fabrication of precisely engineered nanostructures owing to their atomically precise near-spherical structures.

## REFERENCES AND NOTES

1. A. W. Castleman Jr., S. N. Khanna, *J. Phys. Chem. C* **113**, 2664–2675 (2009).
2. H. Häkkinen, *Chem. Soc. Rev.* **37**, 1847–1859 (2008).
3. F. Lips, R. Clérac, S. Dehnen, *Angew. Chem. Int. Ed.* **50**, 960–964 (2011).
4. J.-Q. Wang, S. Stegmaier, T. F. Fässler, *Angew. Chem. Int. Ed.* **48**, 1998–2002 (2009).
5. M. Ruck, V. Dubensky, T. Söhnel, *Angew. Chem. Int. Ed.* **42**, 2978–2982 (2003).
6. H. W. Kroto, J. R. Heath, S. C. O'Brien, R. F. Curl, R. E. Smalley, *Nature* **318**, 162–163 (1985).
7. W. Kratschmer, L. D. Lamb, K. Fostiropoulos, D. R. Huffman, *Nature* **347**, 354–358 (1990).
8. K. Tanigaki *et al.*, *Nature* **352**, 222–223 (1991).
9. X. Lu, L. Feng, T. Akasaka, S. Nagase, *Chem. Soc. Rev.* **41**, 7723–7760 (2012).
10. J. Zhao, Q. Du, S. Zhou, V. Kumar, *Chem. Rev.* **120**, 9021–9163 (2020).
11. S. Aoyagi *et al.*, *Nat. Chem.* **2**, 678–683 (2010).
12. C. M. Beavers *et al.*, *J. Am. Chem. Soc.* **133**, 15338–15341 (2011).
13. S. Stevenson *et al.*, *Nature* **401**, 55–57 (1999).
14. M. J. Moses, J. C. Fetting, B. W. Eichhorn, *Science* **300**, 778–780 (2003).
15. S. C. Sevoj, J. D. Corbett, *Science* **262**, 880–883 (1993).
16. M. P. Johansson, D. Sundholm, J. Vaara, *Angew. Chem. Int. Ed.* **43**, 2678–2681 (2004).
17. S. Kenzler *et al.*, *Angew. Chem. Int. Ed.* **58**, 5902–5905 (2019).
18. S.-F. Yuan, C.-Q. Xu, J. Li, Q.-M. Wang, *Angew. Chem. Int. Ed.* **58**, 5906–5909 (2019).
19. J. Tillmann *et al.*, *Angew. Chem. Int. Ed.* **54**, 5429–5433 (2015).
20. W. I. F. David *et al.*, *Nature* **353**, 147–149 (1991).
21. K. Exner, P. von Ragué Schleyer, *Science* **290**, 1937–1940 (2000).
22. M. Lein, J. Frunzke, G. Frenking, *Angew. Chem. Int. Ed.* **42**, 1303–1306 (2003).
23. M. Westerhausen, S. Weinrich, P. Mayer, *Z. Anorg. Allg. Chem.* **629**, 1153–1156 (2003).
24. H. Breunig, R. Rösler, *Coord. Chem. Rev.* **163**, 33–53 (1997).
25. S. C. Critchlow, J. D. Corbett, *Inorg. Chem.* **23**, 770–774 (1984).
26. Y. Wang *et al.*, *J. Am. Chem. Soc.* **139**, 619–622 (2017).
27. I. A. Popov *et al.*, *Angew. Chem. Int. Ed.* **55**, 15344–15346 (2016).
28. F.-X. Pan *et al.*, *J. Am. Chem. Soc.* **137**, 10954–10957 (2015).
29. X. Kang, H. Chong, M. Zhu, *Nanoscale* **10**, 10758–10834 (2018).
30. H. Yang *et al.*, *Nat. Commun.* **4**, 2422–2429 (2013).
31. D. Y. Zubarev, A. I. Boldyrev, *Phys. Chem. Chem. Phys.* **10**, 5207–5217 (2008).
32. T. Lu, F. Chen, *J. Comput. Chem.* **33**, 580–592 (2012).
33. N. V. Tkachenko, I. A. Popov, A. Muñoz-Castro, *Eur. J. Inorg. Chem.* **41**, 4239–4250 (2021).
34. N. Fedik, A. I. Boldyrev, A. Muñoz-Castro, *Phys. Chem. Chem. Phys.* **21**, 25215–25219 (2019).
35. C. Foroutan-Nejad, *Theor. Chem. Acc.* **134**, 8 (2015).
36. R. Islas, T. Heine, G. Merino, *Acc. Chem. Res.* **45**, 215–228 (2012).

## ACKNOWLEDGMENTS

We are grateful for the valuable discussions with X.-B. Wang (PNNL), J. Xu (NKU), and N. Li (Rigaku Beijing Co., Ltd.). **Funding:** This work was supported by the National Natural Science Foundation of China (nos. 92161102 and 22371140), the Natural Science Foundation of Tianjin City (no. 21JCZJC00140), and 111 project (B18030) from China (MOE). A.M.-C. acknowledges financial support from ANID FONDECYT Regular 1221676. **Author contributions:** Conceptualization: Z.-M.S.; Methodology: A.M.-C. and Z.-M.S.; Investigation: Y.-H.X.; Visualization: Y.-H.X., W.-J.T., A.M.-C., and Z.-M.S.; Funding acquisition: A.M.-C. and Z.-M.S.; Project administration: Z.-M.S.; Supervision: Z.-M.S.; Writing – original draft: Y.-H.X., W.-J.T., A.M.-C., and Z.-M.S.; Writing – review and editing: Y.-H.X., W.-J.T., A.M.-C., G.F., and Z.-M.S. **Competing interests:** The authors declare no competing interests. **Data and materials availability:** X-ray data are available free of charge from the Cambridge Crystallographic Data Centre under reference numbers CCDC 2269174 (method 1) and 2291088 (method 2). All other experimental, spectroscopic, crystallographic, and computational data are included in the supplementary materials. **License information:** Copyright © 2023 the authors, some rights reserved; exclusive licensee American Association for the Advancement of Science. No claim to original US government works. <https://www.science.org/about/science-licenses-journal-article-reuse>

## SUPPLEMENTARY MATERIALS

[science.org/doi/10.1126/science.adj6491](https://science.org/doi/10.1126/science.adj6491)  
Materials and Methods  
Figs. S1 to S9  
Tables S1 to S6  
References (37–53)

Submitted 8 July 2023; resubmitted 3 September 2023  
Accepted 4 October 2023  
10.1126/science.adj6491